



Calculation of Station-Representative Isotropic Receiver Functions

SEONGRYONG KIM^{1,2} and JUNKEE RHIE¹ 

Abstract—The estimation of one-dimensional (1-D) isotropic structures is routine work in most receiver function (RF) analyses that generally use a reference radial RF (RRF) for each station. However, the assumption of negligible back-azimuthal dependencies in a set of RRFs for a station may not be valid because of anisotropic layering, dipping structures, or incorrect sensor orientations. This work presents a comprehensive procedure to obtain a station-representative isotropic RRF, which can be applied automatically to prepare RRF data. The method incorporates a harmonic stripping method with a grid-search for sensor orientations. An optimum angle for the sensor orientation is determined by searching for the angle that minimizes the energy in the tangential component RF (TRF). For each searched angle, possible effects by anisotropy and dipping structures are iteratively suppressed by an inversion process to exclude two- and four-lobe back-azimuthal patterns. The performance of the method was first confirmed with a test using a set of highly noisy composite RRFs and TRFs. The method was then applied to RF data from the southern Korean Peninsula and southwestern Japan. Obtained isotropic RRFs and measured station orientations were found to be reliable in comparisons with results from neighboring stations and previous studies. As an automatized routine pre-process, the obtained isotropic RRF data are particularly useful for estimating 1-D isotropic structures in migration or inversion studies, which are potentially affected by back-azimuthal dependencies in RF data calculated through conventional averaging methods.

Key words: Isotropic receiver function, harmonic stripping, station orientation, Korean Peninsula, F-net.

1. Introduction

Receiver function (RF) analysis (Langston 1979; Owens et al. 1984; Randall 1989; Ammon et al. 1990; Zhu and Kanamori 2000) is one of the primary

practices used to investigate crustal and upper mantle structures (e.g., thickness of layers, V_S variation, and V_P/V_S ratio), beneath seismic stations, and the method has been routinely applied, particularly for stations in newly deployed seismic arrays (e.g., USArray Transportable Array). By deconvolutions of the radial component with the vertical component of incoming teleseismic waveforms at a station (i.e., radial receiver function; hereafter, RRF), source effects can be minimized and converted signals at certain discontinuities (e.g., P-to-S conversion at the Moho; see Fig. 1 for the ray path geometry) are enhanced. Inverse modelling (e.g., Ammon et al. 1990) approaches have been mainly applied to the RRFs, and the methods generally use one or a few station-averaged RRFs to estimate a representative isotropic one-dimensional (1-D) structural model beneath the station. However, the process is highly non-linear (Ammon et al. 1990) and, therefore, care must be taken to prevent the results from being affected by errors in input data that can potentially originate from local anisotropy or incorrect orientations of sensors.

In an isotropic medium, the signal deconvolved from the tangential component with the vertical component (i.e., tangential receiver function; hereafter, TRF) is null because of the absence of converted energy from incident P-wave signals to transverse directions (Fig. 1). Several studies (Levin and Park 1998; Shiomi and Park 2008) show that specific harmonic patterns of signals will appear in the TRF when anisotropic or dipping layers exist beneath the station. Because the signals in the TRF depend on the back-azimuth (Levin and Park 1998), they can be extracted and suppressed by harmonic stripping procedures (e.g., Bianchi et al. 2010; Shen et al. 2013). In addition, incorrect orientations of the horizontal components of the sensor (i.e., aligned to north, N, and east, E, directions as shown in Fig. 1)

¹ School of Earth and Environmental Sciences, Seoul National University, Gwanak-ro 1, Gwanak-gu, Seoul 08826, Republic of Korea. E-mail: rhie@snu.ac.kr

² Present Address: Department of Geology and Earth Environmental Sciences, Chungnam National University, Daehak-ro 99, Yuseong-gu, Daejeon 34134, Republic of Korea.

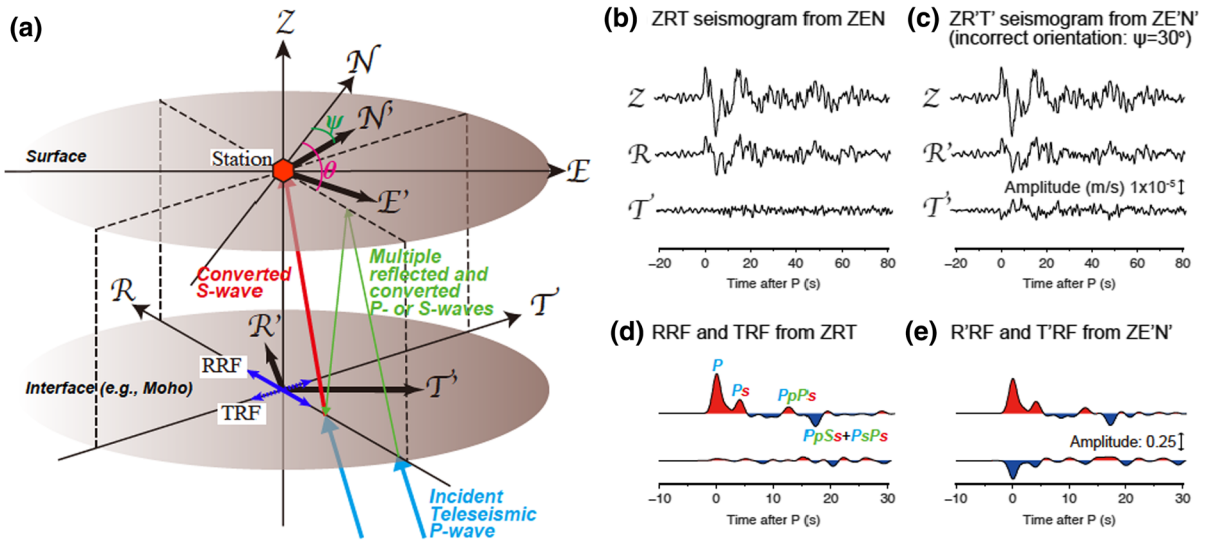


Figure 1

a Schematic plot of the coordinate systems for the converted S-wave (red arrowed line) and reflected and converted P- and S-waves (green arrowed lines) from the incident teleseismic P-wave (light blue arrowed lines) with an angle of back-azimuth (θ). The letters E, N, Z, R, and T indicate east, north, vertical, radial, and tangential directions, respectively. The primed coordinate system E', N', R', and T' (bold arrows) shows an example with an incorrect sensor orientation N' and E' (rotated clockwise by the angle of ψ). Two-sided arrows in blue show polarized particle motions of radial (RRF) and tangential (TRF) receiver functions. **b** and **c** A schematic seismograms of P-wave and following phases from a teleseismic event for the correct (Z, R, and T) and incorrect (Z, R', and T') sensor orientations, respectively. **d** and **e** Calculated RRF (upper traces) and TRF (bottom traces) waveforms from corresponding seismograms in **b** and **c** respectively. The first P-wave arrival, conversions (Ps), and following multiples (color-coded following the schematic rays in **a**) are indicated with letters on the RRF waveform in **d**

can produce systematic biases in the TRF depending on the back-azimuth. Seismic sensors can be incorrectly aligned to the N and E as a result of limitations during deployment, such as in the cases of ocean bottom seismometers (OBSs) (e.g., Agius et al. 2017) or borehole seismometers. Several approaches have been proposed to correct the sensor orientation by using waveforms of teleseismic first arrivals (Jurkevics 1988; Schulte-Pelkum et al. 2001) and surface waves (Ekström and Busby 2008; Zha et al. 2013).

In this study, we use the property of the RF to minimize the effects of the back-azimuthal dependencies caused by the incorrect orientation of seismometers and structural anisotropy in the calculation of RF waveforms representing the 1-D isotropic structure beneath stations. Essentially, the method searches for an orientation angle for the horizontal component directions that minimizes the amplitudes of signals in the TRF. The rotation procedure incorporates harmonic stripping to extract an isotropic RRF waveform, and the isotropic RRF is

obtained throughout the process by using an ensemble of RRFs and TRFs from teleseismic earthquakes in different back-azimuths. Our approach has several potential advantages compared with previous methods for orientation correction or RF selections to obtain average RFs per station, and these advantages are as follows. (1) The process can be systematically carried out without pre-processing (e.g., manual picking or visual data selection) to prepare station-representative RF data for later inversion or stacking analyses. (2) Possible effects by complex earthquake source forms and anisotropic structures are suppressed in the process. (3) The obtained isotropic RRF provides a quick way to image structures beneath a station by migration or inversion techniques. Lastly, (4) effects of anisotropy or dipping layers beneath the station (Olugboji and Park 2016) can be estimated using residual waveforms of the harmonic analysis (see more details in Sect. 2). To demonstrate the performance of this approach, we apply the method to observed data from broadband

networks in the Korean Peninsula and in Kyushu and nearby islands in Japan; these networks incorporate borehole stations and are located near subducting oceanic slabs.

2. Theory and Method

2.1. Source Equalization Process for an Arbitrarily Oriented Seismic Station

The RF is calculated by the source equalization procedure (Langston 1979), which removes the effects of the source and the near-source propagation. Assuming an incoming plane P-wave (Fig. 1), the RRF and TRF are defined by deconvolution of the vertical component, U_Z , from the radial and tangential components, U_R and U_T , respectively (Ammon 1991). In the spectral domain with frequency ω , the RRF and TRF are expressed as follows:

$$RRF(\omega) = \frac{U_R(\omega)}{U_Z(\omega)} \text{ and } TRF(\omega) = \frac{U_T(\omega)}{U_Z(\omega)}. \quad (1)$$

Note that TRF is theoretically zero due to the lack of tangential particle motion in the incoming P-wave (Fig. 1) assuming an isotropic medium.

In the case of an incorrect orientation of horizontal components, we assume primed components as observations of radial, $U_{R'}$, and tangential, $U_{T'}$, components, which are recorded with an incorrectly oriented sensor to the N' and E' , i.e., rotated clockwise by the angle of ψ from the true N and E (Fig. 1). Then, the observed signals have a rotational relationship as shown below:

$$\begin{bmatrix} U_R \\ U_T \end{bmatrix} = \begin{bmatrix} \cos \psi & -\sin \psi \\ \sin \psi & \cos \psi \end{bmatrix} \begin{bmatrix} U_{R'} \\ U_{T'} \end{bmatrix}. \quad (2)$$

The RRF and TRF with the correct orientation can be calculated from the signals with an incorrect orientation ψ by the relationship between Eqs. (1) and (2) as follows:

$$\begin{aligned} RRF(\omega, \psi) &= \frac{U_{R'}(\omega) \cos \psi - U_{T'}(\omega) \sin \psi}{U_Z(\omega)} \text{ and} \\ TRF(\omega, \psi) &= \frac{U_{R'}(\omega) \sin \psi + U_{T'}(\omega) \cos \psi}{U_Z(\omega)}, \end{aligned} \quad (3)$$

and in the time domain,

$$\begin{aligned} RRF(t, \psi) &= \cos \psi RRF'(t) - \sin \psi TRF'(t) \text{ and} \\ TRF(t, \psi) &= \sin \psi RRF'(t) + \cos \psi TRF'(t). \end{aligned} \quad (4)$$

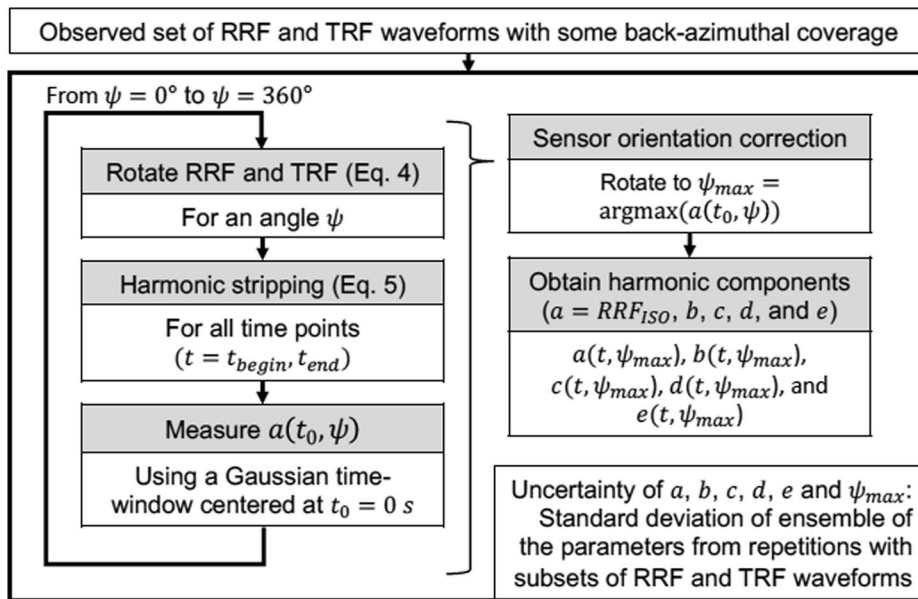
Here, RRF' and TRF' indicate the deconvolved signals of $U_{R'}(t)$ and $U_{T'}(t)$ with $U_Z(t)$, respectively.

2.2. Estimation of Isotropic RF by Harmonic Decomposition

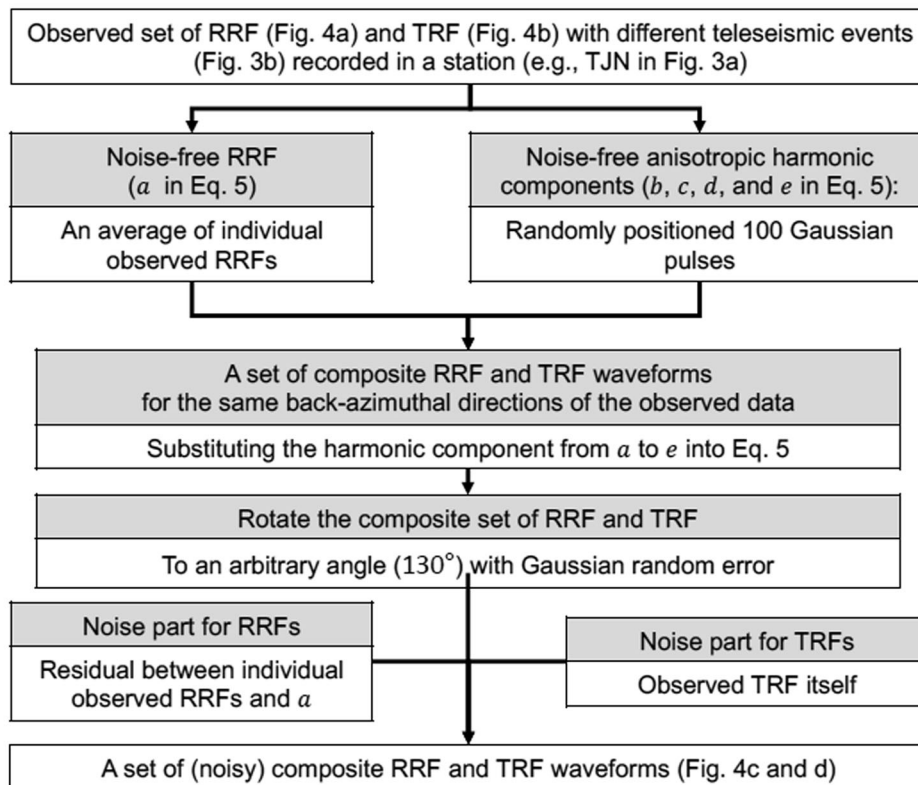
In an anisotropic medium, there is back-azimuth dependency of the energy partitioning by the P-to-S conversion from the incoming P-wave that affects amplitudes and polarities of phases in the RRF and TRF (e.g., Levin and Park 1998; Shiomi and Park 2008). The conversion of P-wave to transverse S-wave across an anisotropic structure forms a systematic pulse shape with an azimuthal dependency (Levin and Park 1998). In the case of a dipping isotropic layer or an anisotropic layer with a tilted symmetry axis, the dependency shows a two-lobed pattern. On the other hand, a four-lobed pattern indicates an anisotropic layer with a horizontal symmetry axis. Based on the properties, an ensemble of pairs of the RRF and TRF from different teleseismic sources can be decomposed with a linear system of the harmonic relationships (e.g., Bianchi et al. 2010; Ologboji and Park 2016):

$$\begin{bmatrix} RRF_1(t, \psi) \\ TRF_1(t, \psi) \\ \vdots \\ RRF_N(t, \psi) \\ TRF_N(t, \psi) \end{bmatrix} = \begin{bmatrix} 1 & \cos \theta_1 & \sin \theta_1 & \cos 2\theta_1 & \sin 2\theta_1 \\ 0 & \cos(\theta_1 + \frac{\pi}{2}) & \sin(\theta_1 + \frac{\pi}{2}) & \cos(2\theta_1 + \frac{\pi}{4}) & \sin(2\theta_1 + \frac{\pi}{4}) \\ \vdots & \vdots & \vdots & \vdots & \vdots \\ 1 & \cos \theta_N & \sin \theta_N & \cos 2\theta_N & \sin 2\theta_N \\ 0 & \cos(\theta_N + \frac{\pi}{2}) & \sin(\theta_N + \frac{\pi}{2}) & \cos(2\theta_N + \frac{\pi}{4}) & \sin(2\theta_N + \frac{\pi}{4}) \end{bmatrix} \begin{bmatrix} a(t, \psi) \\ b(t, \psi) \\ c(t, \psi) \\ d(t, \psi) \\ e(t, \psi) \end{bmatrix}, \quad (5)$$

(a) Procedure to obtain the isotropic radial RF and anisotropic components



(b) Procedure to generate a set of composite RRF and TRF



◀Figure 2

Flow charts to summarize **a** the grid-search based harmonic procedure to obtain the isotropic RRF and anisotropic components (Sect. 2), and **b** the procedure to generate a composite RRF and TRF dataset used in the test of the method (Sect. 4)

where the back-azimuth of each event is θ , and the indexes indicate earthquake numbers for the total N sources. By solving the linear system for each time-point, we obtain decomposed isotropic and harmonic components in the vector of the right-hand side of the system, which are diagnostics of the isotropic (a), two-lobed (2π -periodicity) anisotropic (b and c), and four-lobed (π -periodicity) anisotropic (d and e) medium.

2.3. Calculation of a Station-Representative RF

The isotropic component a at a certain time does not contribute to the back-azimuthal dependency, but it is a function of the orientation angle ψ , that is because of the assumption that the energy partitioning of the incoming P-wave energy is entirely governed by the harmonic components in Eq. (5). Hence, the value of the orientation angle can be estimated by means of searching for an angle with the maximum amplitude of the function a . With the searched angle, therefore, the harmonic stripping process in Eq. (5) ensures that the function a is the RF response of the isotropic structure. Consequently, the isotropic RRF representative at a station can be estimated by:

$$RRF_{ISO}(t) = a(t, \operatorname{argmax}(a(t_0, \psi))), \quad (6)$$

where the operator argmax indicates an argument value of ψ at which the function a is maximized at $t = t_0$.

We use a grid-search method to find $\operatorname{argmax}(a(t_0, \psi))$ in Eq. (6). The angle ψ is changed from 0° to 360° with 2° spacings. In the proposed method, the following steps are carried out (Fig. 2a). (1) For a given angle, the matrix (Eq. 5) is inverted by using the LSQR algorithm (Paige and Saunders 1982) to obtain isotropic (a) and harmonic components (b , c , d , and e). (2) A Gaussian time-window is applied to estimate the amplitude of a (centered at $t_0 = 0$ s). The standard deviation of the window can

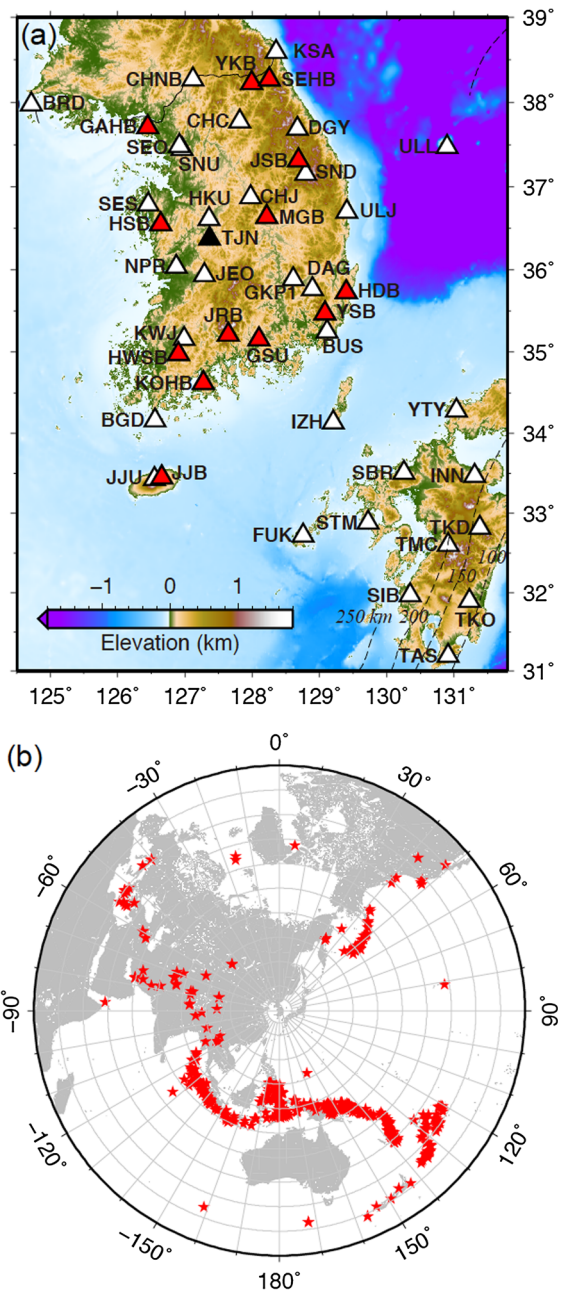


Figure 3

a Map of broadband stations (triangles) in the southern Korean Peninsula (35 stations) and in Kyushu and nearby islands in Japan (11 stations). Note that the black triangle indicates the station in Daejeon (TJN) for which the RF data were used to produce synthetic data in the synthetic test (Fig. 4). Total 13 borehole stations in the Korean Peninsula are marked with red triangles. **b** Map showing event locations (red stars) used in receiver function calculations

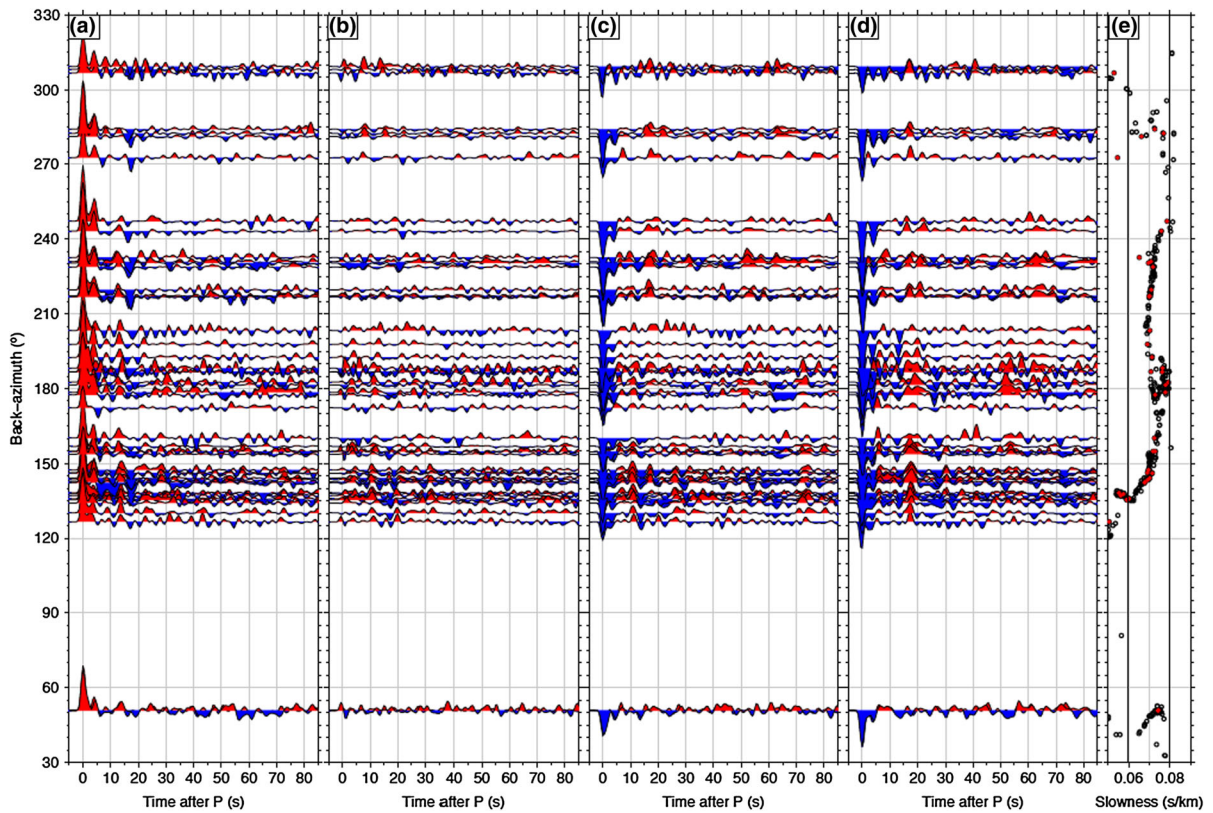


Figure 4

Examples of observed **a** RRF and **b** TRF waveforms at the TJN station sorted with respect to the back-azimuth; **c** and **d** show respectively the same as **a** and **b**, but for the synthetic generated RRF and TRF as described in the main text and Fig. 2b. **e** Values of slowness are presented (circles filled with red) at the corresponding back-azimuth. Two vertical lines at 0.06 and 0.08 indicate the range of slowness used in this study. Note that the presented examples in **a–d** are randomly selected 50 RRF and TRF waveforms out of total 531 data, where corresponding values of slowness and back-azimuth are indicated in **e** with hollow circles

be varied based on the frequency content of RF waveforms. (3) The steps (1) and (2) are repeated for all angles, and the angle with a maximum amplitude of a is selected and RRF_{ISO} is obtained. To quantify uncertainties on RRF_{ISO} , a Jackknife test (Efron and Stein 1981) is performed 100 times in steps from (1) to (3) by resampling iteratively the subset (the third quarter) of the entire set of individual RFs.

3. RF Data

The presented method was tested by using observed RF data of broadband networks in the southern Korean Peninsula and Japan (Fig. 3a). Those networks have been operated by the Korean Meteorological Administration (KMA) and Korea

Institute of Geoscience and Mineral Resources (KIGAM) in the Korean Peninsula. In addition, F-net broadband stations (Okada et al. 2004) managed by the National Research Institute for Earth Science and Disaster Resilience (NIED) in Kyushu and nearby islands in Japan were used to check the performance of the method for regions where strong anisotropy and dipping interfaces are anticipated by the subducting Philippine Sea oceanic slab (Fig. 3a). The KMA and KIGAM stations consist of ground and borehole sensors, and the F-net stations consist of ground stations.

We used 531 teleseismic event data between 2005 and 2012 in the distance and magnitude ranges of 30° – 95° and $M5.5$ – 7.0 , respectively (Fig. 3b). Following the workflow of Tauzin et al. (2017), more than 300 RFs were computed but depending of

recording conditions the numbers per station vary. The RF waveforms were calculated by using a time-domain iterative deconvolution method (Ligorria and Ammon 1999). We used 1.0 of the Gaussian width factor in the deconvolution process. The signal-to-noise ratio (SNR) was measured with raw waveforms before the RF calculation, and low-quality data (SNR < 3.0) were discarded. Note that no further systematic process was performed to control the quality of data. Examples of RF waveforms for the TJN station are presented in Fig. 4. The RF waveforms generally showed good quality where the first P arrivals and crustal phases are clearly identified in the RRF (Fig. 4a) with a relatively quiet TRF pair (Fig. 4b).

4. Test of the Method using a Composite RF Dataset

Before the application with observed RF data, we tested the method by using a set of composite RF data to demonstrate the recovery of input isotropic and harmonic component waveforms (Fig. 5). The dataset of composite RRF and TRF waveforms were formed based on the observed waveforms at the TJN station in Korea (Fig. 3a) instead of calculating synthetic waveforms. With the purpose of testing the systematic harmonic procedure in Sect. 2, this approach is conducted as a simple and quick way not only to account for complexities in the data and their noise but also to avoid difficulties in calculating actual responses of a structural velocity model. The summary of the approach is illustrated in Fig. 2b. First, an average waveform of observed RRFs was assumed to be the RRF_{ISO} component. Second, the anisotropic harmonic components ($b-e$ in Eq. 5) were constructed by using waveforms generated with randomly positioned 100 Gaussian pulses (with random amplitudes between 0.01 and -0.01 , and the value of standard deviation corresponding to the used Gaussian width factor). Third, a set of RRF and TRF waveforms were produced for the same set of back-azimuthal directions of the observed data (Fig. 4e) by using the matrix relationship in Eq. (5). Fourth, the effect caused by an incorrect sensor orientation was applied by rotating the produced RRF and TRF waveforms 130° counter-clockwise. Gaussian

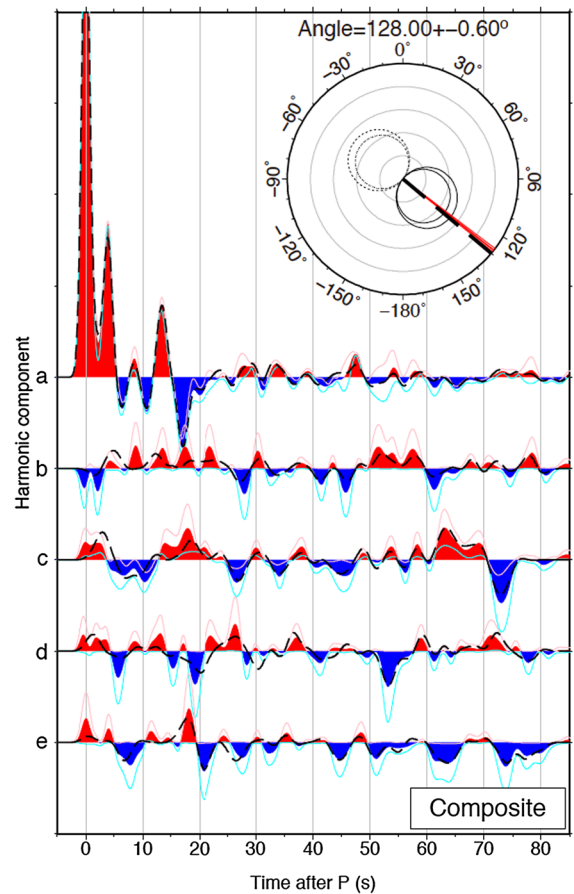


Figure 5

Results of the recovery test using composite data (see main text for details). The isotropic and harmonic components from “a” to “e” are defined in Eq. (5). The component “a” indicates the isotropic RRF. The harmonic component “b, c” and “d, e” show two- and four-lobed pattern of anisotropy (see Sect. 2.2 for further information). The positive and negative picks of waveforms are filled with red and blue, respectively. Hair lines in pink and cyan indicate ± 1 standard deviation ranges. Input waveforms are superimposed with dashed lines. The inset shows the estimated station orientation and its ± 1 standard deviation uncertainties (red lines). The bold dashed line is the input orientation. Four gray circles indicate the amplitude of the $\text{argmax}(a(t_0, \psi))$ in Eq. (6) from 0.2, 0.4, 0.6, and 0.8 from the center (0.0) of the inset circle (1.0). The range of estimated ± 2 standard deviations of the amplitude is presented as a function of the rotation angle with solid (positive amplitude) and dashed (negative amplitude) lines

random error with $\pm 2.5^\circ$ standard deviations of the orientation was added for each set of RRF and TRF. Lastly, realistic composite RRFs (Fig. 4c) and TRFs (Fig. 4d) were formed by adding noise. For the noise part of the RRF waveforms, we used residual signals by subtracting the average waveform (RRF_{ISO} in

Table 1

Measured sensor orientations and comparisons with previous studies

Network name	Station name	Number of RFs	Sensor orientation (°)	Standard deviation (°)	Lee and Rhie (2015)		Lee and Sheen (2015)	
					Sensor orientation (°)	Difference to this study (°)	Sensor orientation (°)	Difference to this study (°)
F-net	FUK	374	2	2.5768	–	–	–	–
F-net	INN	393	2	1.0392	–	–	–	–
F-net	IZH	378	– 2	1.9287	–	–	–	–
F-net	SBR	386	0	0.6325	–	–	–	–
F-net	SIB	374	2	2.1354	–	–	–	–
F-net	STM	385	2	2.506	–	–	–	–
F-net	TAS	380	2	1.8974	–	–	–	–
F-net	TKD	236	0	3.0067	–	–	–	–
F-net	TKO	366	2	3.9547	–	–	–	–
F-net	TMC	391	0	4.0694	–	–	–	–
F-net	YTY	379	4	1.99	–	–	–	–
KIGAM	BGD	348	2	1.2962	1	1	–	–
KIGAM	CHNB	310	– 16	0.6325	– 20	4	–	–
KIGAM	GKP1	366	– 6	4.1713	– 5	1	–	–
KIGAM	^a GSU	364	– 142	1.918	– 135	7	– 156.7	14.7
KIGAM	^a HDB	207	– 164	16.18	– 178	14	– 135.9	28.1
KIGAM	HKU	367	– 10	1	– 7	3	–	–
KIGAM	^a HSB	281	148	3.945	130	18	132.4	15.6
KIGAM	^a HWSB	210	– 56	3.5327	– 58	2	– 66.9	10.9
KIGAM	^a JJB	221	126	0.959	125	1	124.2	1.8
KIGAM	^a JRB	281	164	1.673	166	2	168.9	4.9
KIGAM	^a JSB	264	116	3.795	115	1	117.5	1.5
KIGAM	KSA	327	– 4	5.099	– 10	6	–	–
KIGAM	^a MGB	323	– 110	3.476	– 132	22	– 134.2	24.2
KIGAM	NPR	237	– 2	1.7321	2	4	–	–
KIGAM	SND	384	0	0.2828	–	–	–	–
KIGAM	SNU	326	– 6	0.3464	–	–	–	–
KIGAM	TJN	376	0	1.7321	–	–	–	–
KIGAM	^a YKB	258	164	3.323	–	–	178.8	14.8
KIGAM	^a YSB	154	– 16	1.2166	–	–	– 12.5	3.5
KMA	BRD	271	– 4	1.8655	– 3	1	–	–
KMA	BUS	229	– 8	1.249	– 10	2	–	–
KMA	CHC	218	– 8	3.1623	– 5	3	–	–
KMA	CHJ	224	– 10	1.6852	– 8	2	–	–
KMA	DAG	171	– 4	2.0396	– 9	5	–	–
KMA	DGY	161	– 12	2.2804	– 10	2	–	–
KMA	^a GAHB	99	– 128	1.51	– 129	1	– 131.2	3.2
KMA	JEO	100	– 2	2.623	–	2	–	–
KMA	JJU	215	– 4	1.2961	– 5	1	–	–
KMA	^a KOHB	37	176	2.919	–	–	174.9	1.1
KMA	KWJ	225	– 6	2.4576	–	–	–	–
KMA	^a SEHB	62	– 14	7.5842	93	107	– 73.6	59.6
KMA	SEO	215	– 2	1	– 5	3	–	–
KMA	SES	195	– 4	1.99	0	4	–	–
KMA	^a SMKB	10	– 6	22.653	– 5	1	– 3	3
KMA	ULJ	166	0	3.1241	– 1	1	–	–
KMA	ULL	161	– 10	9.6229	– 165	155	–	–

^aBorehole stations

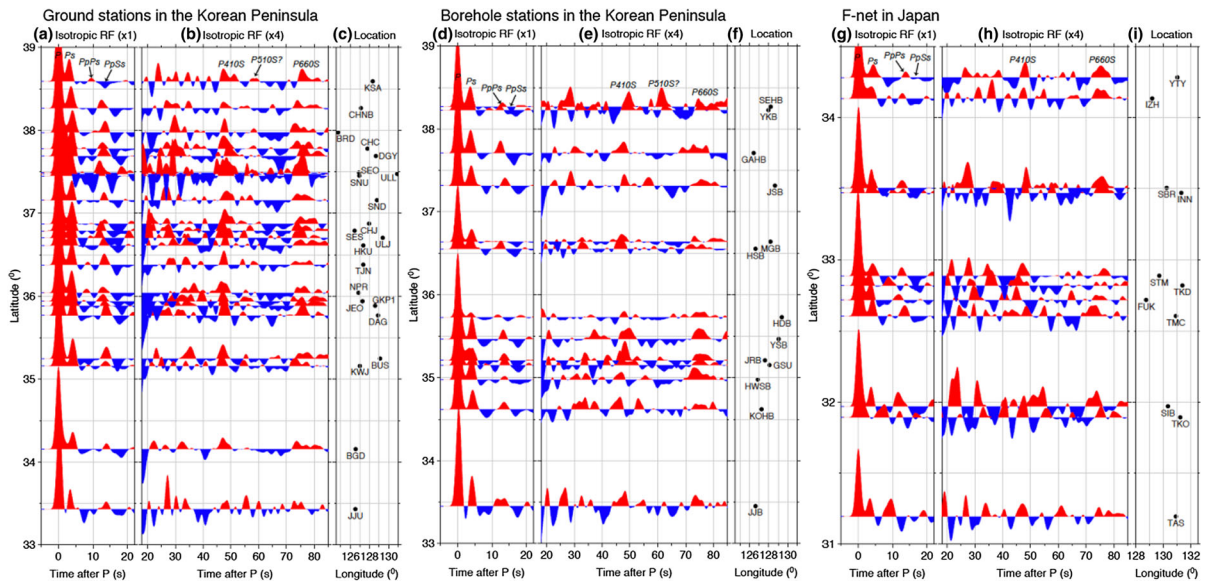


Figure 6

Isotropic RRFs calculated by using observed data for the stations in Fig. 2a. **a, d** and **g** Isotropic RRFs in the time-window between -5 and 22 s show crustal phases. **b, e** and **h** The same isotropic RRFs in a different time-window (18 – 85 s) show phases from the upper mantle transition zone. Note that the amplitude of signals is exaggerated four times. **c, f** and **i** Geographical locations of corresponding stations with their names

Fig. 5) from the individual observed RRFs (Fig. 4a). The observed TRFs (Fig. 4b) were directly used for the noise of the composite TRFs. It can be observed in Fig. 4c, d that the finally obtained composite RF waveforms were highly complex, despite the fact that the signals were produced from a common RRF_{ISO} waveform.

Figure 5 shows RRF_{ISO} and other harmonic components (b – e) estimated from the composite RRF and TRF. The test results show that the assumed input signals were well recovered particularly in RRF_{ISO} and the later part of the harmonic components (> 20 s). Our additional testing without noise showed an almost identical recovery, and this indicates that relatively less recovery in the earlier part of the harmonic components was due to the applied strong noise in the orientation and waveforms. Nevertheless, the estimated waveforms were highly comparable to input signals. The amount of estimated uncertainties was not affected much by the phase of signals, but mainly depended on the amplitudes of signals. The estimated rotation angle was -128.0 ± 0.6 , which was close to the assumed rotation. The small deviation from the input angle could have been due to the

non-uniform back-azimuthal coverage and input noises.

5. Applications to Real Data

The method was applied to RRFs from stations in the southern part of the Korean Peninsula and the southwestern part of Japan (Fig. 3a). The number of RRFs finally used in the analysis of each station is presented in Table 1.

5.1. Estimation of Isotropic RRFs

Obtained isotropic RRFs show clear picks, and their arrival times are coherent among neighboring stations. In particular, converted phases at discontinuities in depth can be clearly identified, including not only crustal phases (e.g., P-to-S conversion at the Moho interface and its multiples), but also upper mantle phases (P-to-S conversions at 410 and 660 upper mantle discontinuities) (Fig. 6). The RRFs from stations on the islands (JJU and ULL) and in the region above the subducting slab (F-net stations) depict more complex patterns with strong

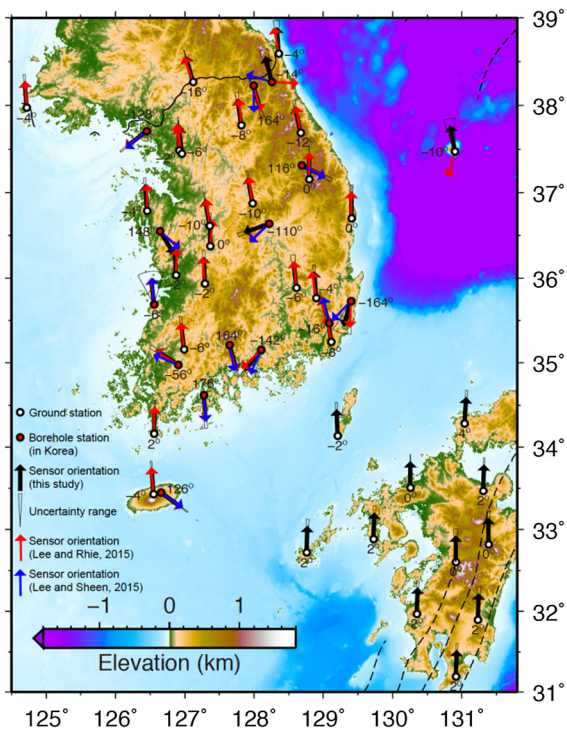


Figure 7

Map showing sensor orientations estimated in this study (black arrows) and from previous studies by Lee and Rhie (2015) (red arrows) and Lee and Sheen (2015) (blue arrows) in the region. White and red circles indicate locations of ground and borehole stations

positive and negative reverberations. Nevertheless, obtained isotropic RFs are similar to them in other neighboring stations in terms of timing and shape of the crustal and mantle phases.

5.2. Sensor Orientations

Estimated sensor orientations highly vary in borehole stations compared to ground stations (Fig. 7 and Table 1). To check the reliability, our orientation measurements were compared with two previous independent studies by using the P-wave polarity (Lee and Sheen 2015) and ambient noise correlation (Lee and Rhie 2015) data (Fig. 7 and Table 1). Lee and Rhie (2015) used the Rayleigh ellipticity properties to determine the sensor orientation (Zha et al. 2013). The orientations measured in ground stations agreed well with previous measurements, and the variations did not exceed $\pm 5^\circ$. The ULL is a station that showed a significant difference

(155°) compared to the measurement using ambient noise data (Lee and Rhie 2015). The authors of the previous studies reported that their estimations may be less reliable for stations at distal locations from the center of the used array (Figs. 3a, 7). Accounting for the fact that the sensor is installed on the ground at the station, our measurement (-10°) is more acceptable. This indicates that the presented method can be used in a complementary way with other methods. Notably, F-net stations are generally well oriented to the north, and this corresponds to the station information (0° for all stations) reported by NIED, although the stations are situated near the subducting Philippine Sea slab.

Orientations of some borehole sensors in Korea (GSU, HDB, HSB, MGB, YKB, and SEHB) differed ($> 10^\circ$) from the previous estimations (Table 1). The discrepancy was mainly due to changes of orientations during the replacement or maintenance of sensors. For instance, KIGAM reported a change of the sensor in 2010 for MGB (Hyun-Moo Cho in KIGAM, personal communication) that corresponds to the sudden change of the estimated orientation with a large uncertainty (Fig. 8). However, Lee and Rhie (2015) and Lee and Sheen (2015) used data for shorter time periods (2007–2009 and 2013–2014, respectively) compared to the longer data length of this study (2005–2012). We performed the same yearly tests for the borehole stations. At HDB, HSB, YKB, and SEHB, a similar abrupt change was observed during 2010, 2007, 2006, and 2010, respectively.

5.3. Anisotropic Harmonic Properties

As indicated in Eq. (5), anisotropic harmonic properties are simultaneously estimated in the process. Figure 9 shows examples of estimated isotropic and anisotropic components for the TJN, JJB, and TKO stations. It has been generally reported that subducting oceanic lithospheres result in strong anisotropy (e.g., Shimi and Park 2008). Amplitudes of the anisotropic components are higher at TKO (Fig. 9c) than at TJN (Fig. 9a) because TJN is located on a relatively homogeneous continental crust. Station JJB (Fig. 9b) displays anisotropic components with similar amplitudes to those of TKO. This

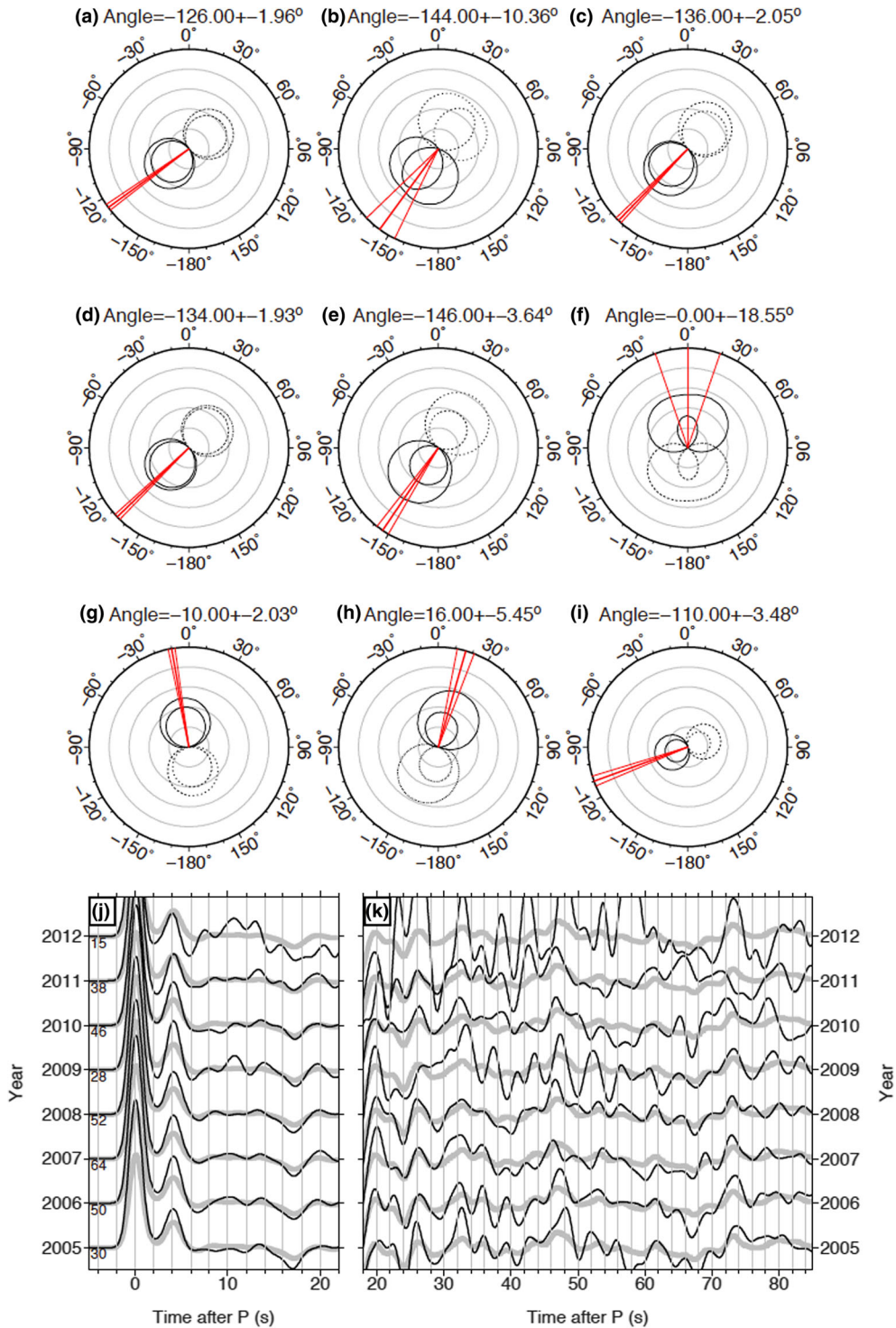


Figure 8

Results of the yearly test for the sensor orientation of MGB (Fig. 3a). **a-h** Sensor orientations estimated using 1-year data from 2005 to 2012, respectively. The convention is the same with the inset in Fig. 4. They are compared to the case using **i** all data. Corresponding isotropic RRFs are presented in **j** for crustal phases and **k** for mantle phases as in Fig. 5

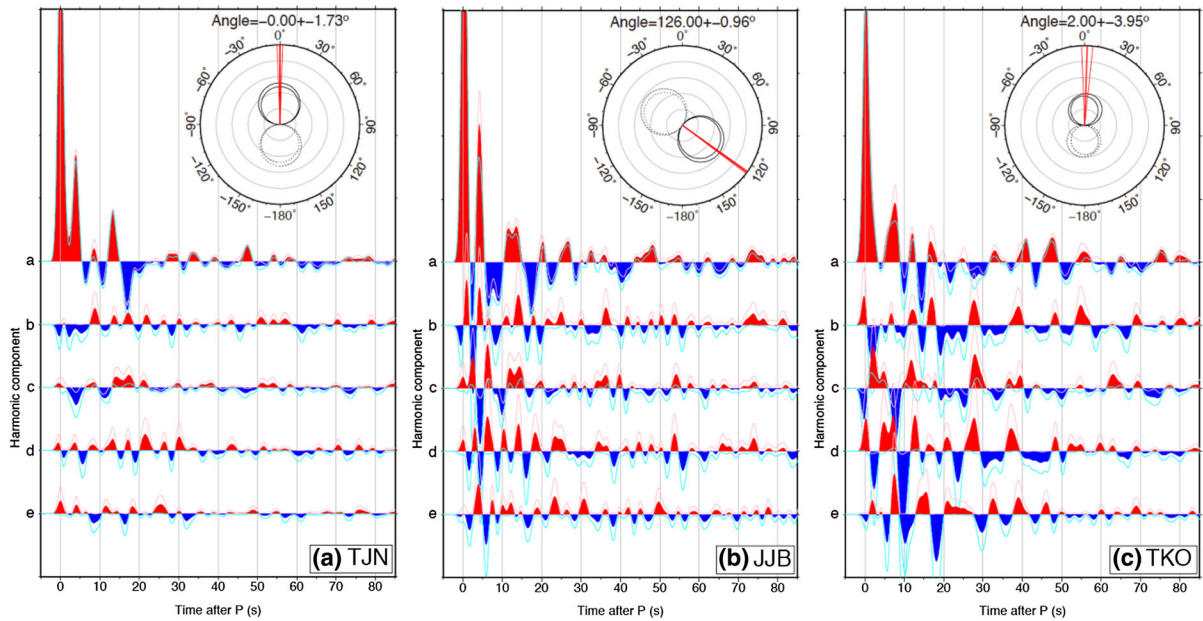


Figure 9

Isotropic and anisotropic harmonic component of receiver functions for stations **a** TJN, **b** JJB and **c** TKO

indicates that the crustal and upper mantle structure beneath the island (Fig. 3a) is likely more anisotropic compared to the main land of Korea. Station TKO displays strong phases in anisotropic components that appear 40–50 s after the beginning. In contrast, phases at times earlier than 20 s have higher amplitudes than later parts in the anisotropic components of JJB. It is possible to draw a simple interpretation from the observation that possible structures causing anisotropic wave propagations are located at shallower depths beneath JJB than TKO. Strong positive picks were coherently observed at 27 s in *b–d* only beneath TKO, which is a phenomenon that was not observed in the isotropic RRF. Though further analysis is required, this could indicate the effect of the sub-crustal dipping oceanic slab beneath the station.

5.4. Application to RFs with Higher Frequency Contents

We additionally applied the presented method to higher frequency RF data, which were obtained by using 2.5 of the Gaussian width factor. Figure 10 shows an example of the applications to ULL, where

more complex signals can be anticipated by strong reverberations in the highly complicated structure (Fig. 6a, b). Obtained isotropic and anisotropic component waveforms from the high frequency RF data (Fig. 10b) were more complex, but agreed well with the features for the lower frequency results (Fig. 10a) in terms of the timing of distinctive phases. The orientation estimated from the higher frequency RF was -8° . The estimation corresponds to the results from the low frequency RF, and the estimated uncertainty was even smaller in the higher frequency.

5.5. Potential Applications of the Method

The obtained RF from application of the method (Eq. 6) represents the responses of average 1-D isotropic structures beneath a station derived by minimizing possible effects of back-azimuthal dependencies due to dipping layers, anisotropic structures, and incorrect sensor orientations. With the increase of dense seismic arrays, two- or three-dimensional isotropic structures can thus be readily imaged by an ensemble of systematically processed results from a set of RRFs and TRFs using the presented method. For instance, migration techniques can be simply

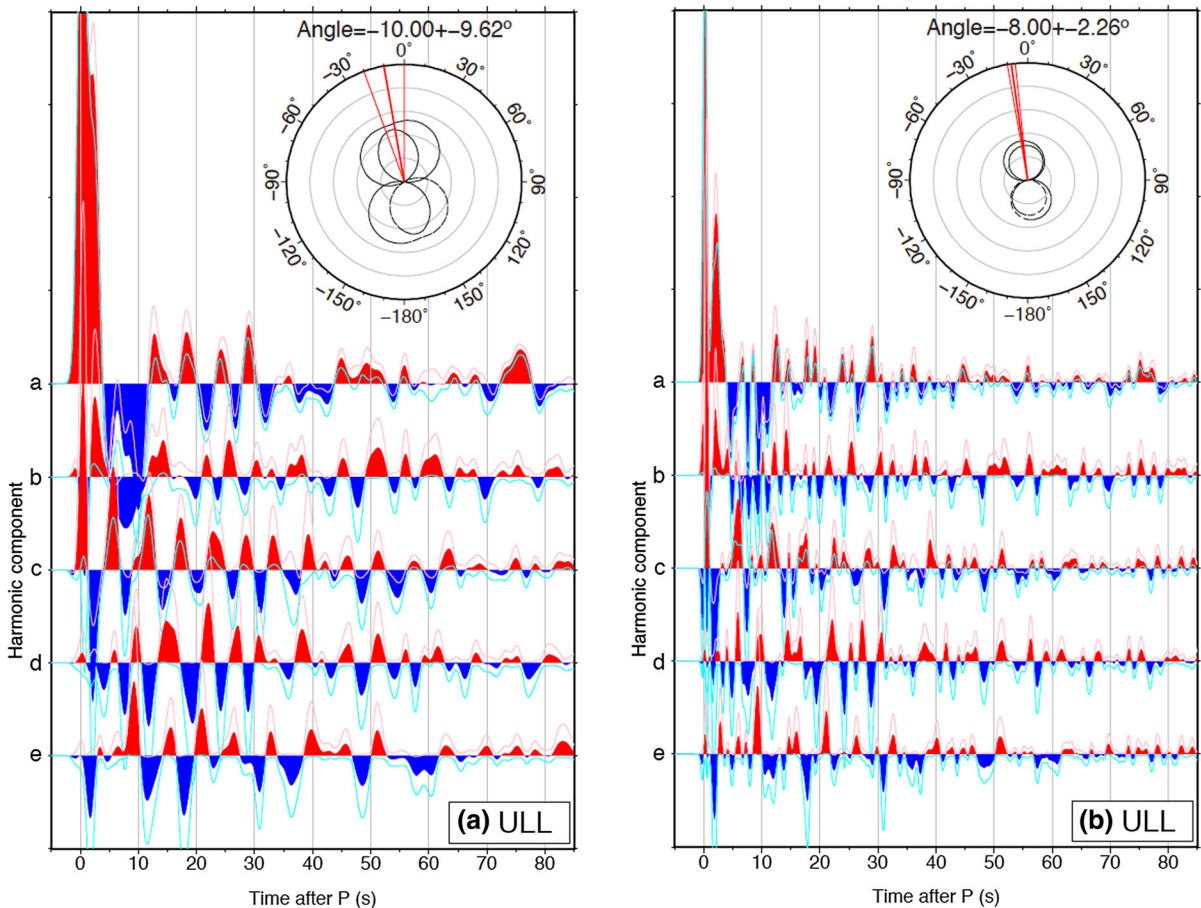


Figure 10

Effect of different frequency content for **a** lower and **b** higher frequency (using 1.0 and 2.5 of the Gaussian with width factor) on the harmonic component of receiver function for station ULL

applied to the obtained RFs to convert the time to the depth. We expect that estimates of not only crustal structures, but also structures in the upper mantle transition zone can be obtained as we observed clear signals from deep depths (Fig. 6).

Another important application of the method is the automatic preparation of RF data for inversions of RRF to estimate 1-D shear-wave velocity structures. Simple stacking of RRFs might not properly suppress the back-azimuthal dependencies, and this could result in some bias in the inversion results. We performed a test to show that inversions using a station-representative RRF from our method can potentially extract more meaningful structures in comparison with the case using the RRF from simple stacking (Fig. 11). To better observe the effect of

differences in input data, we used a fully non-linear Bayesian inversion approach (Kim et al. 2016a), which can reflect data information rigorously by application of transdimensional and hierarchical schemes (e.g., Bodin et al. 2012; Kim et al. 2016a). In the test, the high frequency RF (Figs. 10b and 11e, f) were used together with the RF shown in Fig. 6 at the location of ULL (Fig. 3a) to obtain more stable results. The obtained isotropic RRFs from our method and the simple stacking ones showed small differences (Fig. 11c–f). Nevertheless, estimated models (Fig. 11a, b) showed clear differences at interface depths, including at the Moho and sub-lithospheric boundaries. Relatively less sharp interfaces were estimated in the model that used the stacked RF (Fig. 11b) compared to the model that

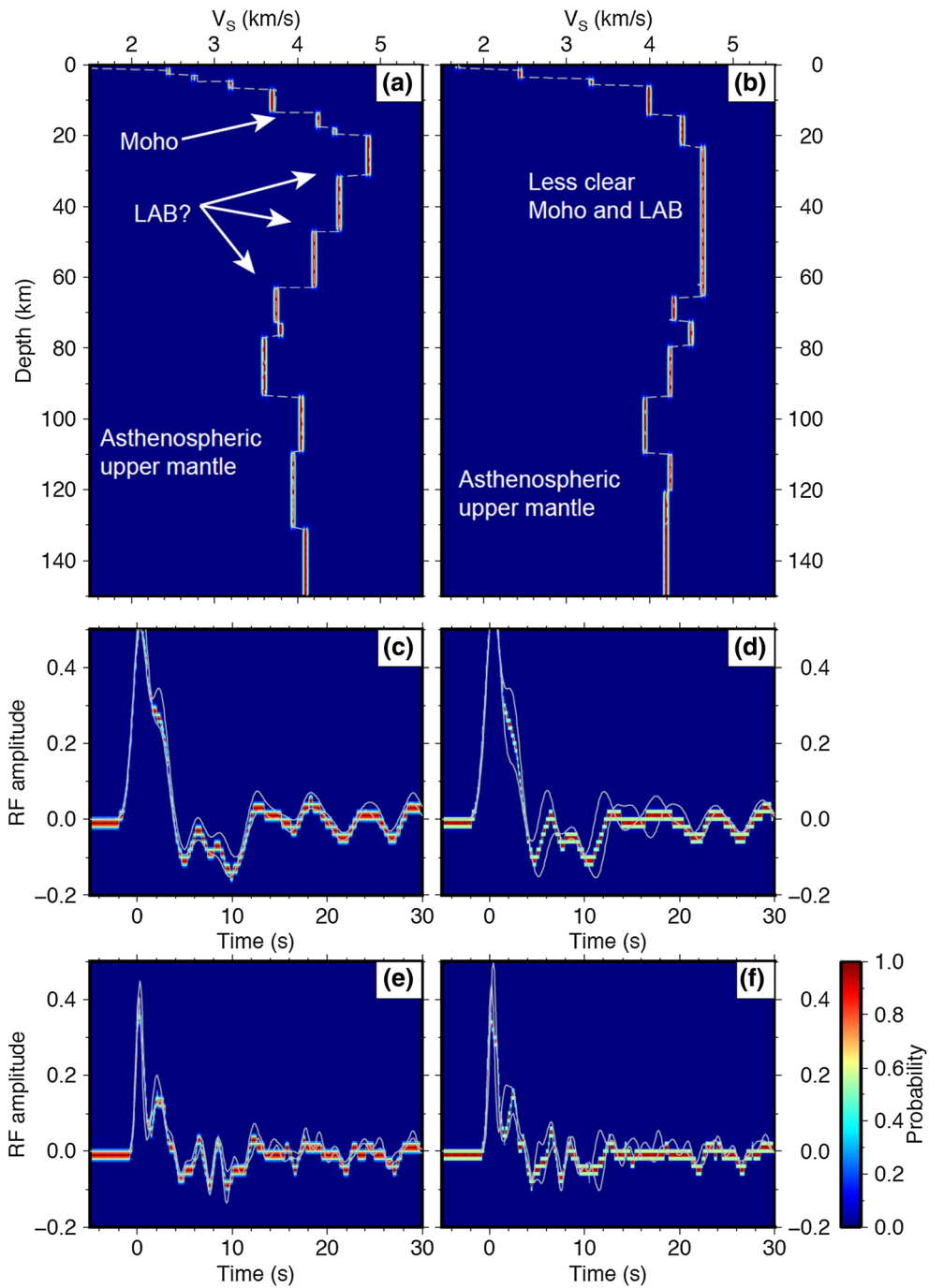


Figure 11

Comparisons of inversion results (posterior probability distribution, PPD) using **a** the isotropic RRF and **b** RRF from simple averaging for ULL. The mean model from the PPD is indicated by dashed gray lines. **c, d** Lower frequency RRFs and **e, f** higher frequency RRFs are presented by their ± 1 standard deviation ranges (gray lines). The background images are PPDs of predicted data for the PPD models in **a** and **b**

used the RF from our method (Fig. 11a). This discrepancy indicates that our method potentially preserves information about the isotropic structure beneath a station, which can be biased by the interference of signals with back-azimuthal dependency. Moreover, this region is known as a rifted continental margin that was formed during the Miocene back-arc spreading event that involved the subducting Pacific slab (Ren et al. 2002). Hence, it is more likely that the lithosphere is not thicker here than that in the nearby Korean Peninsula where the thickness can be as small as 60 km (Pasyanos et al. 2014; Kim et al. 2016b). Therefore, the model employing RRFs from our method produces preferential results based on the tectonic setting, though the exact thickness of the lithosphere is still not clear beneath the island. As indicated by this test, the proposed method can be used in systematic inversion studies with RF data to obtain a set of 1-D models beneath large and dense seismic arrays such as the USArray and F-net.

6. Conclusions

This work presents a method to calculate a representative isotropic RRF for a station from a set of RRFs and TRFs with a certain back-azimuthal coverage. Harmonic stripping is used to suppress possible biases caused by anisotropic structures and dipping layers. Isotropic and anisotropic harmonic components are calculated by inverting the harmonic matrix using the LSQR algorithm. In addition, the method incorporates a grid-search procedure to account for incorrect sensor alignments of horizontal components to the N and E directions. The harmonic stripping procedure is performed for every searched orientation angle. Over the entire set of evaluated angles, the representative isotropic RRF is obtained by taking the isotropic component that minimizes and maximizes energy in the TRF and RRF, respectively. Uncertainties are estimated through a random sampling test, and the whole process is repeated 100 times by using the resampled third quarter of all data.

The performance of the method was first tested by using a set of composite RRF and TRF waveform data, which were rotated to a specific angle and

included realistic errors taken from observed data at station TJN. The obtained isotropic RRF and anisotropic components agreed well with the input waveforms. Then, we applied the method to observed RFs from stations in the southern Korean Peninsula (the KIGAM and KMA networks) and in the southwestern part of F-net. Estimated isotropic RRFs showed coherent phase arrivals of the crustal and the upper mantle discontinuities among neighboring stations. The orientation angles agreed well with those in previous reports and studies. In particular, our orientation measurements may be potentially more stable for stations where strong interference of noise is anticipated. The comparison of inversion results between station-representative RRFs obtained through our method and a simple stacking one revealed that the isotropic RRF from our method can contain more information that can be resolved in inversions. The presented method is performed in a fully automatic manner, and in turn, it can be applied systematically to prepare station-representative isotropic RRFs for imaging structures beneath large and highly dense arrays.

Acknowledgements

The authors are appreciative of Benoit Tauzin and Jung-Ung Woo for valuable discussions about the method. This work was supported by the Korea Institute of Energy Technology Evaluation and Planning (KETEP) and the Ministry of Trade, Industry & Energy (MOTIE) of the Republic of Korea (No. 20132510100060). We used data from broadband stations operated by the Korea Institute of Geoscience and Mineral Resources, Korea Meteorological Administration, and F-net.

Publisher's Note Springer Nature remains neutral with regard to jurisdictional claims in published maps and institutional affiliations.

REFERENCES

Agius, M. R., Rychert, C. A., Harmon, N., & Laske, G. (2017). Mapping the mantle transition zone beneath Hawaii from Ps

- receiver functions: Evidence for a hot plume and cold mantle downwellings. *Earth Planetary Science Letters*, 474, 226–236. <https://doi.org/10.1016/j.epsl.2017.06.033>.
- Ammon, C. J. (1991). The isolation of receiver effects from teleseismic P waveforms. *Bulletin-Seismological Society of America*, 81(6), 2504–2510.
- Ammon, C. J., Randall, G. E., & Zandt, G. (1990). On the nonuniqueness of receiver function inversions. *Journal of Geophysical Research: Solid Earth*, 95(B10), 15303–15318. <https://doi.org/10.1029/JB095iB10p15303>.
- Bianchi, I., Park, J., Piana Agostinetti, N., & Levin, V. (2010). Mapping seismic anisotropy using harmonic decomposition of receiver functions: An application to Northern Apennines, Italy. *Journal of Geophysical Research: Solid Earth*, 115(B12), B12317. <https://doi.org/10.1029/2009JB007061>.
- Bodin, T., Sambridge, M., Tkalčić, H., Arroucau, P., Gallagher, K., & Rawlinson, N. (2012). Transdimensional inversion of receiver functions and surface wave dispersion. *Journal of Geophysical Research: Solid Earth*, 117(B2), B02301. <https://doi.org/10.1029/2011JB008560>.
- Efron, B., & Stein, C. (1981). The jackknife estimate of variance. *The Annals of Statistics*, 9(3), 586–596. <https://doi.org/10.1214/aos/1176345462>.
- Ekström, G., & Busby, R. W. (2008). Measurements of seismometer orientation at USArray Transportable Array and Backbone stations. *Seismological Research Letters*, 79(4), 554–561. <https://doi.org/10.1785/gssrl.79.4.554>.
- Jurkevics, A. (1988). Polarization analysis of three-component array data. *Bulletin of the Seismological Society of America*, 78(5), 1725–1743.
- Kim, S., Dettmer, J., Rhie, J., & Tkalčić, H. (2016a). Highly efficient Bayesian joint inversion for receiver-based data and its application to lithospheric structure beneath the southern Korean Peninsula. *Geophysical Journal International*, 206(1), 328–344. <https://doi.org/10.1093/gji/ggw149>.
- Kim, S., Tkalčić, H., Rhie, J., & Chen, Y. (2016b). Intraplate volcanism controlled by back-arc and continental structures in NE Asia inferred from transdimensional Bayesian ambient noise tomography. *Geophysical Research Letters*, 43(16), 8390–8398. <https://doi.org/10.1002/2016GL069483>.
- Langston, C. A. (1979). Structure under Mount Rainier, Washington, inferred from teleseismic body waves. *Journal of Geophysical Research: Solid Earth*, 84(B9), 4749–4762. <https://doi.org/10.1029/JB084iB09p04749>.
- Lee, S.-J., & Rhie, J. (2015). Determining the orientations of broadband stations in south Korea using ambient noise cross-correlation. *Geophysics and Geophysical Exploration*, 18(2), 85–90. <https://doi.org/10.7582/GGE.2015.18.2.085>. (in Korean with English abstract).
- Lee, H., & Sheen, D.-H. (2015). A study on determination of orientation of borehole seismometer. *Journal of the Geological Society of Korea*, 51(1), 93. <https://doi.org/10.14770/jgsk.2015.51.1.93>. (in Korean with English abstract).
- Levin, V., & Park, J. (1998). P-SH conversions in layered media with hexagonally symmetric anisotropy: A cookbook. *Pure and Applied Geophysics*, 151(2–4), 669–697. <https://doi.org/10.1007/s000240050136>.
- Ligorria, J. P., & Ammon, C. J. (1999). Iterative deconvolution and receiver-function estimation. *Bulletin of the Seismological Society of America*, 89(5), 1395–1400.
- Okada, Y., Kasahara, K., Hori, S., Obara, K., Sekiguchi, S., Fujiwara, H., et al. (2004). Recent progress of seismic observation networks in Japan—Hi-net, F-net, K-NET and KiK-net. *Earth, Planets and Space*, 56(8), xv–xxviii.
- Olugboji, T. M., & Park, J. (2016). Crustal anisotropy beneath Pacific Ocean-Islands from harmonic decomposition of receiver functions. *Geochemistry, Geophysics, Geosystems*, 17(3), 810–832. <https://doi.org/10.1002/2015GC006166>.
- Owens, T. J., Zandt, G., & Taylor, S. R. (1984). Seismic evidence for an ancient rift beneath the Cumberland Plateau, Tennessee: A detailed analysis of broadband teleseismic Pwaveforms. *Journal of Geophysical Research: Solid Earth*, 89(B9), 7783–7795. <https://doi.org/10.1029/JB089iB09p07783>.
- Paige, C. C., & Saunders, M. A. (1982). LSQR: An algorithm for sparse linear equations and sparse least squares. *ACM Transactions on Mathematical Software (TOMS)*, 8(1), 43–71.
- Pasyanos, M. E., Masters, T. G., Laske, G., & Ma, Z. (2014). LITHO1.0: An updated crust and lithospheric model of the Earth. *Journal of Geophysical Research: Solid Earth*, 119(3), 2153–2173. <https://doi.org/10.1002/2013jb010626>.
- Randall, G. E. (1989). Efficient calculation of differential seismograms for lithospheric receiver functions. *Geophysical Journal International*, 99(3), 469–481. <https://doi.org/10.1111/j.1365-246X.1989.tb02033.x>.
- Ren, J., Tamaki, K., Li, S., & Junxia, Z. (2002). Late Mesozoic and Cenozoic rifting and its dynamic setting in Eastern China and adjacent areas. *Tectonophysics*, 344(3–4), 175–205. [https://doi.org/10.1016/S0040-1951\(01\)00271-2](https://doi.org/10.1016/S0040-1951(01)00271-2).
- Schulte-Pelkum, V., Masters, G., & Shearer, P. M. (2001). Upper mantle anisotropy from long-period P polarization. *Journal of Geophysical Research: Solid Earth*, 106(B10), 21917–21934. <https://doi.org/10.1029/2001JB000346>.
- Shen, W., Ritzwoller, M. H., Schulte-Pelkum, V., & Lin, F. C. (2013). Joint inversion of surface wave dispersion and receiver functions: a Bayesian Monte-Carlo approach. *Geophysical Journal International*, 192(2), 807–836. <https://doi.org/10.1093/gji/ggs050>.
- Shiomi, K., & Park, J. (2008). Structural features of the subducting slab beneath the Kii Peninsula, central Japan: Seismic evidence of slab segmentation, dehydration, and anisotropy. *Journal of Geophysical Research: Solid Earth*, 113(B10), B10318. <https://doi.org/10.1029/2007JB005535>.
- Tauzin, B., Kim, S., & Kennett, B. L. N. (2017). Pervasive seismic low-velocity zones within stagnant plates in the mantle transition zone: Thermal or compositional origin? *Earth and Planetary Science Letters*, 477, 1–13. <https://doi.org/10.1016/j.epsl.2017.08.006>.
- Zha, Y., Webb, S. C., & Menke, W. (2013). Determining the orientations of ocean bottom seismometers using ambient noise correlation. *Geophysical Research Letters*, 40(14), 3585. <https://doi.org/10.1002/grl.50698>.
- Zhu, L., & Kanamori, H. (2000). Moho depth variation in southern California from teleseismic receiver functions. *Journal of Geophysical Research: Solid Earth*, 105(B2), 2969–2980. <https://doi.org/10.1029/1999JB900322>.